

Ranges of Rn evaporation residues produced in the $^{16}\text{O} + ^{194}\text{Pt}$ reaction

R. N. Sagaidak,^{1,*} N. A. Kondratiev,^{1,†} L. Corradi,² E. Fioretto,² G. Montagnoli,³ F. Scarlassara,³ and A. M. Stefanini²

¹*Flerov Laboratory of Nuclear Reactions, Joint Institute for Nuclear Research, RU-141980 Dubna, Russia*

²*INFN, Laboratori Nazionali di Legnaro, I-35020 Legnaro (Padova), Italy*

³*Dipartimento di Fisica e Astronomia, Università di Padova, and INFN, Sez. di Padova, I-35131 Padova, Italy*



(Received 17 October 2018; published 7 January 2019)

Ranges for heavy atoms of evaporation residues (ERs) produced in nuclear fusion-evaporation reactions induced by accelerated heavy ions have been systematically considered. New range data obtained for α -emitting short-lived Rn nuclei produced in the $^{16}\text{O} + ^{194}\text{Pt}$ fusion-evaporation reaction have been obtained. These data were derived by the comparison of mean α -particle energies of Rn-isotopes detected in experiments with the Monte Carlo simulations of these energies for the same isotopes stopped in the rotating Al catcher foil. As the result of this procedure applied to the production of ^{206}Rn to ^{203}Rn in the reaction, the ranges obtained in our experiments are 1.65 times larger than those expected from SRIM/TRIM calculations/simulations. To obtain an agreement of the predictions with the experimental data for such heavy atoms at low energies their electronic and/or nuclear stopping power components should be reduced.

DOI: [10.1103/PhysRevC.99.014602](https://doi.org/10.1103/PhysRevC.99.014602)

I. INTRODUCTION

The irregular impact of the projectile atomic number Z_p on the stopping powers (SPs) and ranges of heavy ions (HIs) still remains an open question. This effect (so-called Z_p oscillations) is observed for HI energy-loss measurements in carbon foils at low velocities [1]. The later data [2] obtained at the HI velocity $V = 0.8v_0$ (v_0 is the Bohr velocity) did not reveal these oscillations for $Z_p > 40$ but showed about the same SP values for Nb to Au and some growth from Au to U, at least for HIs used in the experiments, as one can see in Fig. 1 taken from Ref. [3]. Thus, observed Z_p oscillations in SPs were explained by the atomic shell structure of HIs [4]. TRIM simulations [5] [the most popular Monte Carlo (MC) code used for the estimates of HI energy losses and ranges in matter] demonstrate some excess over SPs measured for $40 < Z_p < 60$ [2] and a significant increase in the simulated values for HIs with $Z_p > 62$. Better agreement of the simulations with the data is only achieved with the selection of HIs passed through a carbon foil in a forward direction, as indicated in Fig. 1. At the same time, SRIM (the analytical version of similar estimates) [5] gives SP values that are about three times as large as those obtained in the measurements for $Z_p \geq 70$ (see Fig. 1). The detection of HIs in forward direction, after their passage through an absorber, implies that main energy losses proceed due to the electronic interaction of the projectile and target atoms. In spite of this selection in the experiments, the contribution of the nuclear component to the measured energy losses is estimated at 4 to 28% (see Table 1 in Ref. [1]). However, in spite of the better repro-

duction of the Z_p dependence in TRIM simulations with the angular selection for HIs with $Z_p > 62$, the carbon SP values thus obtained for these HIs still remain overestimated by a factor of up to 2–2.5, as one can see in Fig. 1.

To obtain the electronic SP values, the nuclear stopping (elastic collisions of atoms similar to the collision of billiard balls) is usually calculated analytically followed by its subtraction from the measured SPs, as was done in Refs. [1,2]. SRIM overestimates the nuclear stopping component (and, probably, the electronic one) for heavy atoms with $Z_p > 62$ at low energies, as we can see in Fig. 1. Similar overestimates in SP values were observed at higher energies when comparing the experimental SP data [6,7] to those obtained with SRIM calculations. The nuclear and electronic stopping at low energies were also considered in Refs. [7–9] in more detail.

As for the range measurements, it was found in the systematic range studies performed with the C, B, Be, SiC, and polymer target films that whenever medium-heavy ions are implanted in the energy range from 10 keV to 7.5 MeV, the experimental data [10] are underestimated in the calculations [5] by as much as 40%. The range measurements for heavy radioactive recoils, or evaporation residues (ERs), produced in HI fusion-evaporation reactions allow us to obtain an additional information on stopping of these atoms in solid media. Usually, the range distributions for ERs knocked out from a thin target by HI beam particles are measured with a stack of thin foils followed by the off-line detection of α , β or γ radioactivity of these relatively long-lived reaction products caught by each foil. Forward peaked ER angular distributions and definite kinetic energies determined as $E_{\text{ER}} = E_b A_p A_{\text{ER}} / (A_p + A_t)^2$, where A is the mass number of a projectile and target with indexes p and t , respectively, allow one to obtain the mean ranges at beam energy E_b . For example, the mean ranges of $^{126,128}\text{Ba}$ and ^{142}Sm in Al were

*sagaidak@jinr.ru

†Deceased.

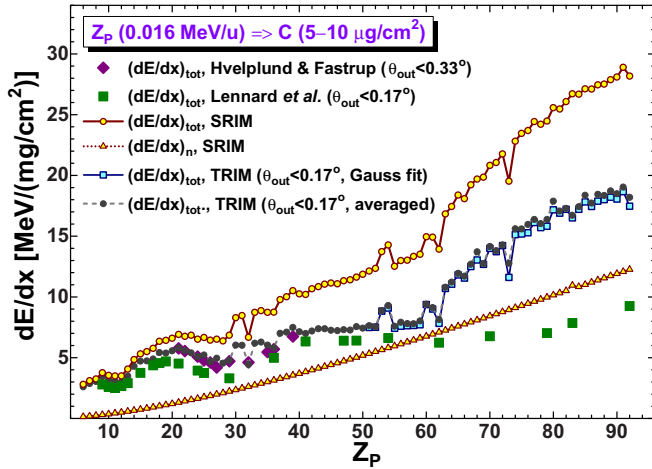


FIG. 1. Carbon SP values for HIs at low energies as obtained in the experiments [1,2] (large full symbols) in comparison with SRIM/TRIM calculations/simulations [5] (small symbols connected by straight lines) [3]. For SRIM calculations, total SP values $(dE/dx)_{\text{tot}}$ and the nuclear SP component $(dE/dx)_n$ are shown. TRIM simulations correspond to the same output angle selection $\theta_{\text{out}} < 0.17^\circ$ for HIs as used in the experiment [2]. Gaussian fits to the energy distributions and their averaging were used to obtain mean energy-loss values.

obtained from their β -activity measurements [11,12]. Similar values for ^{149}Tb and $^{150,151}\text{Dy}$ were obtained by detecting their α particles [13–16]. The comparison of these data with SRIM calculations, as shown in Fig. 2, revealed some overestimate

in the projected ranges calculated for low-energy Ba and Sm ERs (within 10 to 15%) and similar underestimate for those of Tb and Dy (within the same values).

Available data ranges for heavier ERs, which were obtained by detecting their specific γ rays [17–20], reveal a prominent inconsistency with each other, as discovered during their analysis and comparison with SRIM calculations (see Fig. 3). The measured ranges for $^{192-194}\text{Tl}$ and $^{191-193}\text{Hg}$ ERs produced in the $\text{Ta}(^{16}\text{O}, xn)$ and $\text{Ta}(^{16}\text{O}, pxn)$ reactions [20] are about 30% lower than those obtained with SRIM calculations. At the same time, the mean range of $^{192}\text{Tl}/\text{Hg}$ obtained in the $\text{Ta}(^{16}\text{O}, 5n)$ and $\text{Ta}(^{16}\text{O}, p4n)$ reactions at higher beam energies as well as those for $^{188}\text{Au}/\text{Pt}$ obtained in the $^{12}\text{C}+\text{Ta}$ reaction in the same evaporation channels at a lower beam energy [17] exceeds the calculated value by about 20%. The ranges of more energetic ERs from ^{173}Hf to ^{182}Ir , which were produced in the $^{20}\text{Ne}+\text{Ho}$ reaction [19], turned out to be in rather good agreement with those obtained by SRIM, whereas similar low energy ERs produced in the $^{16}\text{O}+\text{Tm}$ reactions [18] revealed ranges that are (30–40)% lower than the calculated ones (see Fig. 3). Note that the measured ranges were corrected for the ERs stopping inside the targets used in the experiments when compared with the calculated ones (bottom panels in Figs. 2 and 3). This correction corresponding to the ER energy losses in a half target thickness, which were calculated with SRIM, had minor values for the thin target data shown in Fig. 2, as well as for the ^{12}C , $^{16}\text{O}+\text{Ta}$ data [17,20] shown in Fig. 3. At the same time, it had appreciable values in the case of the $^{16}\text{O}+\text{Tm}$ and $^{20}\text{Ne}+\text{Ho}$ data [18,19], where rather thick targets were used.

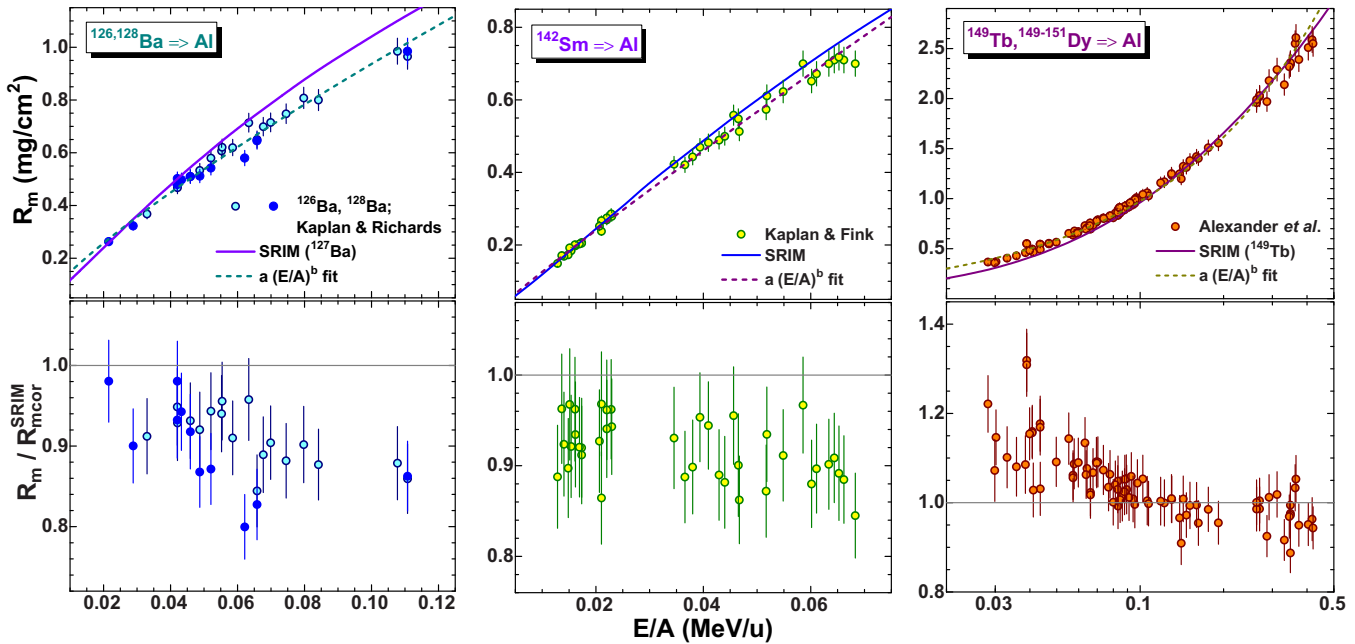


FIG. 2. Mean ranges R_m in Al for $^{126,128}\text{Ba}$ and ^{142}Sm as obtained by their β -activity measurements [11,12], and those for ^{149}Tb and $^{150,151}\text{Dy}$ as obtained by the detection of their α particles [13–16] (circles). All the data shown in upper panels are fitted by the power function (dashed lines) and compared with SRIM calculations [5] (solid lines). Ratios of the measured ranges to the calculated ones corrected for ER stopping inside the targets $R_m / R_{m\text{cor}}^{\text{SRIM}}$ are shown in bottom panels by the same symbols. 5% arbitrary errors are added to the experimental data to get a sense of the significance of the observed deviations.

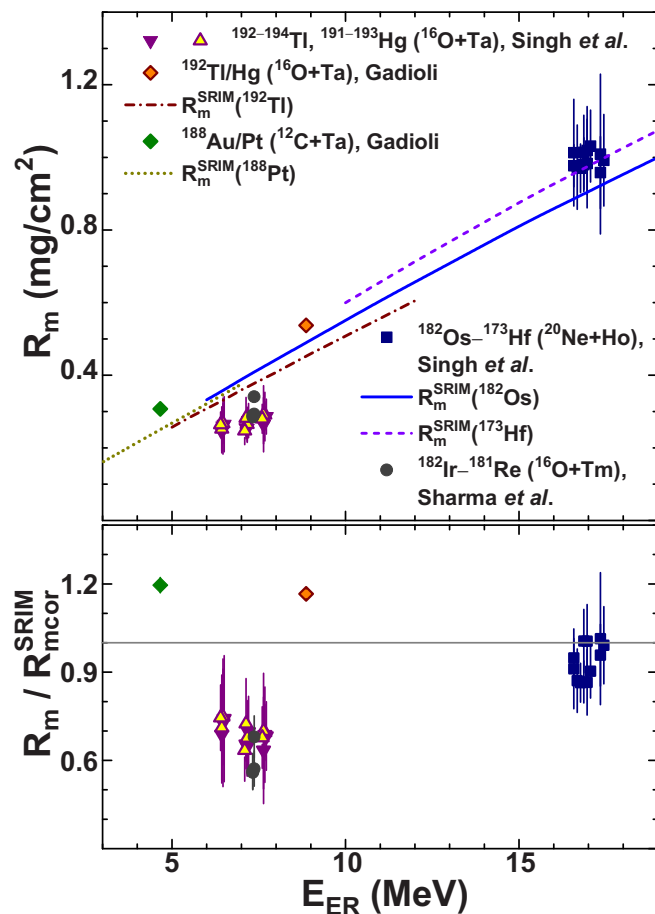


FIG. 3. Mean ranges in Al for Hg and Tl ERs produced in the $^{16}\text{O}+\text{Ta}$ fusion-evaporation reactions as obtained by the detection of γ rays [17,20] (triangles and open diamond). Similar data obtained for $^{188}\text{Au}/\text{Pt}$ produced in the $^{12}\text{C}+\text{Ta}$ reaction [17] and for ERs from ^{182}Ir to ^{181}Re and from ^{182}Os to ^{173}Hf produced in the $^{16}\text{O}+\text{Tm}$ and $^{20}\text{Ne}+\text{Ho}$ reactions [18,19], respectively, are shown by full symbols. SRIM calculations for ranges of corresponding ERs are shown by different lines in upper panel. The ratios of the measured ranges to the calculated ones corrected for ER stopping inside the targets are shown in a bottom panel by the same symbols.

The data comparison for heavier At and Po ERs produced in the $^{16,18}\text{O}+\text{Ir}$ reactions [13,21] reveals larger deviations from the calculated ranges, as shown in Fig. 4. As we can see, the measured ranges exceed the calculated ones by up to 40% at low ER energies. A similar excess is discovered for the $^{210,211}\text{At}$ data obtained in the $^{12}\text{C}+\text{Bi}$ reaction [22] leading to the short-lived $^{218,219}\text{Ac}$ parent nuclei produced in the $3n$ and $2n$ evaporation channels. The analysis of the angular distributions measured in the same work for long-lived $^{210,211}\text{At}$, which was performed in the framework of the approach of Ref. [23] (see below), confirmed their production in the neutron evaporation channels. The data for $^{202,203}\text{Po}$ produced in the $^{12}\text{C}+\text{Au}$ reaction, as obtained by detecting their γ rays [24], are also shown in the figure. We treated the latter data as the results of the fusion-evaporation reactions consisting of their direct production in the $p6n$ and $p5n$ channels along with the contribution from the EC decays

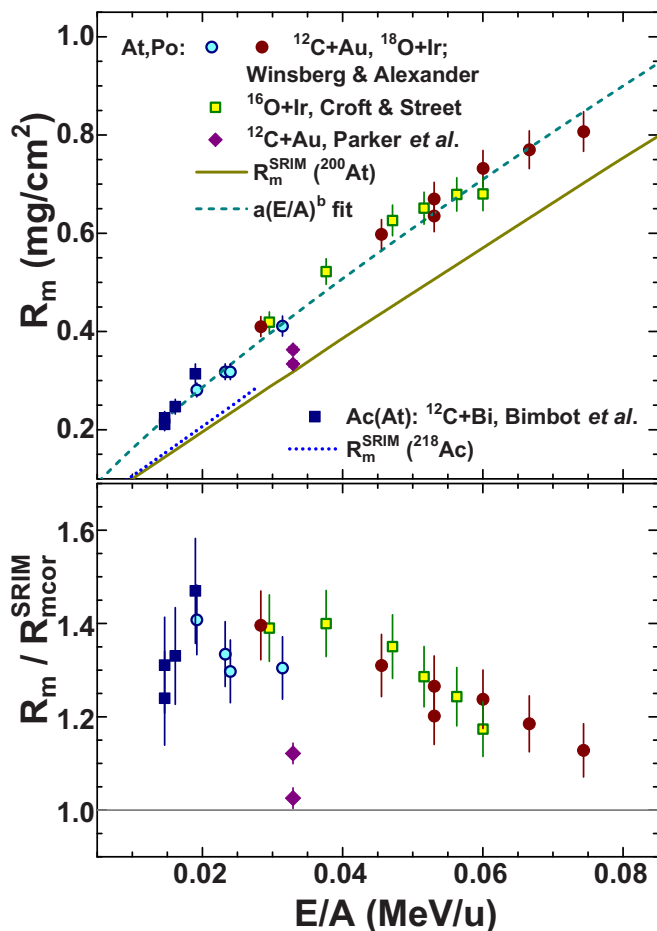


FIG. 4. The same as in Fig. 3, but for the mean ranges of Po and At ERs produced in the $^{12}\text{C}+\text{Au}$ and $^{16,18}\text{O}+\text{Ir}$ reactions, as obtained by the detection of α particles [13,21] (circles and open squares). Similar range data for $^{210,211}\text{At}$ obtained in the $^{12}\text{C}+\text{Bi}$ reaction [22] leading to the short-lived $^{218,219}\text{Ac}$ parent nuclei produced in the $3n$ and $2n$ evaporation channels are shown by full squares. The data for $^{202,203}\text{Po}$ produced in the $^{12}\text{C}+\text{Au}$ reaction, as obtained with the detection of γ rays [24], are shown by full diamonds. See details in the text.

of $^{202,203}\text{At}$ produced in the neutron evaporation channels. Statistical model calculations at the 10 MeV/amu beam energy used in the experiment [24], which were performed with HIVAP [25], yielded cross section values for the At isotopes produced in the $7n$ and $6n$ evaporation channels close to those for the Po isotopes produced in the $p6n$ and $p5n$ channels. In this calculations we optimized the main HIVAP parameters in attempts to reproduce the experimental data on the Au(^{12}C , xn) reaction cross sections [26] at high energies.

As we can see in Figs. 2–4 the ranges obtained for low energy ERs by detecting their α particles [from Tb–Dy up to At(Ac)], are noticeably higher than those calculated with SRIM. Evidently, the reason is the lower SPs of Al than those predicted by SRIM for these heavy atoms. We note that a significant reduction in SPs was observed for low energy heavy atoms in carbon (see Fig. 1). To obtain reliable SP values, a semiempirical approach was proposed for the estimates

of SPs of some solid and gas media [3]. The approach is based on a well-known concept of the effective charge for HIs moving in matter (see, for example, references in Ref. [27]). Thus, for the effective charge of hydrogen, the expression proposed by Ziegler [27] was used. Relative values of the effective charge γ for HIs were obtained from measured SPs as a function of HI reduced velocity V_{red} expressed through relative value of V/v_0 and HI projectile atomic number Z_P as $V_{\text{red}} = (V/v_0)/Z_P^{2/3}$. The parametrization of the HI effective charges was performed with the empirical modification of the Thomas-Fermi expression, $\gamma \equiv (z_H^*/Z_P) = 1 - A \exp(-\lambda V_{\text{red}})$, where z_H^* is the effective charge of the hydrogen ion, and A and λ are the fitting parameters [28]. The fitted curve resulting from this two-parameter function fit to the data (508 data points were used according to the database [29]) reproduced the experimental γ values reasonably well in a wide range of HI energies and Z_P (see Fig. 11 in Ref. [3]). Note that the contributions of the nuclear stopping to the measured SP values were ignored (not subtracted from the measured values) in this approach. Bearing in mind that the HI effective charge is the result of the interaction of the projectile and target atomic electrons, it is thought that this approximation might be not correct at very low HI velocities.

Considering the range data for heavy energetic atoms, one has to mention their importance for clarifying mechanisms of the incomplete fusion (multinucleon transfer) reactions leading to the production of heavy nuclei in HI induced reactions. A number of works was devoted to recognize the mechanism(s) of heavy nuclei formation in noncompound nuclear reactions studied together with the evident production of ERs in the complete fusion with the use of the recoil-range technique [17–20,22,24,30,31]. In this connection, it may be noted that selectivity of the α decay for heavy nuclei detected using the recoil-range technique [13–16,21,22,31,32] leads to more definite results compared to those obtained with the detection of their γ rays, as one can see in Fig. 3.

In this work we present the data on the ranges in Al for short-lived Rn isotopes produced in the $^{16}\text{O} + ^{194}\text{Pt}$ fusion-evaporation reactions at different ^{16}O beam energies. The applicability of the effective charge parametrization [3] mentioned above and TRIM simulations [5] has been also tested in attempts to reproduce the Rn ranges. In Sec. II we describe briefly our experiments on the collection and detection of Rn ERs. Section III is devoted to the simulations used for the data analysis and derivation of the ranges, whereas in Sec. IV we present our results and discuss them. Finally, in Sec. V we summarize the study and make some conclusions that follow from this work.

II. EXPERIMENT

A. Preparatory experiments

In preparatory experiments a ^{241}Am α source was used to check the ability of TRIM simulations to reproduce the energy losses of α particles registered with our spectrometric system using a semiconductor surface-barrier detector (SSBD). In these experiments α particles were detected after their passage through three different “sandwiches” composed from

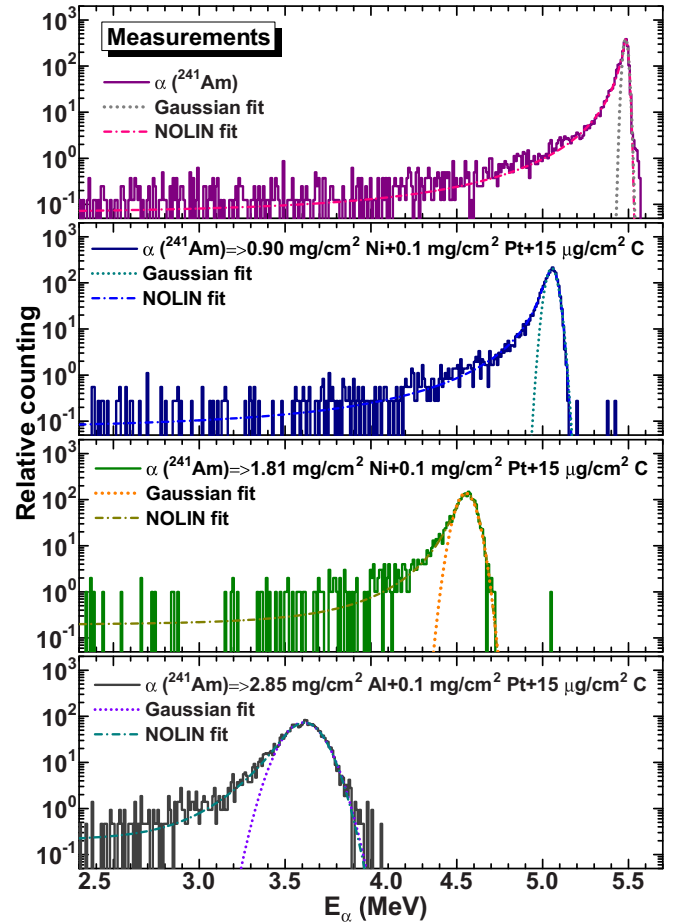


FIG. 5. The α spectra obtained directly with the ^{241}Am α source without any degrader (an upper panel) and with the same α particles passed through the “sandwiches” indicated in lower panels (histograms). The results of fits with the Gaussian and NOLIN functions [34] are shown by dotted and dash-dotted lines, respectively. See details in the text.

the catcher foil (one of the 0.90 mg/cm² Ni, 1.81 mg/cm² Ni, and 2.85 mg/cm² Al foil was used), 0.1 mg/cm² ^{194}Pt target, and the 15 µg/cm² C-foil (target backing). These “sandwiches” were initially prepared for the online detection of α particles from ERs collected by these catchers in the geometry with their detection in backward direction (relatively to the beam) using an annular SSBD [33]. The α spectra obtained directly from the source and those obtained after transmitting through the “sandwiches” were described within two models. The first model implied the 5.486 MeV monoenergy α line and the Gaussian approximation to the α peaks collected in the transmitting experiments. Within this model a mean α -particle energy E_m and full width at half-maximum (FWHM) were estimated. In the second one, the NOLIN model proposed earlier [34] was used to describe the forms of α peaks observed in experiments. It could be done with a “two-Gaussians+hyperbola” function that allowed to describe a low energy “tail” in the observed α -spectrum. E_m and FWHM could be also estimated within this model.

TABLE I. Mean energy E_m and full width at half-maximum FWHM (both in MeV) of α -peaks obtained with the ^{241}Am α -particles passed through the different catchers (absorbers A) coupled with the (Pt+C) targets. The values obtained with the Gaussian and NOLIN function fits to the observed α -peaks are designated by the indexes G and N, respectively. Thicknesses of the absorbers W (in mg/cm^2) are indicated in brackets. These data are compared to the same parameters for α -peaks obtained with TRIM simulations (T) using the mono-energy 5.486 MeV α line and to the similar ones accompanied by an additional spread according to the form of the α peak observed in the measurement without any degrader and fitted with the NOLIN function (TN). Standard errors in the parameter values are indicated by subscripts. See also Figs. 5 and 6.

$A(W)$	Fits to measurements				Simulations			
	E_m^G	FWHM_G	E_m^N	FWHM_N	E_m^T	FWHM_T	E_m^{TN}	FWHM_{TN}
Ni (0.90)	5.0534 _{0.0011}	0.0676 _{0.0019}	5.0597 _{0.0014}	0.0815 _{0.0082}	5.0554 _{0.0002}	0.0421 _{0.0003}	5.0425 _{0.0010}	0.0607 _{0.0018}
Ni (1.81)	4.5523 _{0.0019}	0.1108 _{0.0034}	4.5604 _{0.0023}	0.1121 _{0.0054}	4.6390 _{0.0001}	0.0597 _{0.0002}	4.6227 _{0.0010}	0.0772 _{0.0017}
Al (2.85)	3.6076 _{0.0023}	0.2247 _{0.0043}	3.6156 _{0.0029}	0.2274 _{0.0061}	3.6395 _{0.0001}	0.0810 _{0.0002}	3.6159 _{0.0007}	0.0983 _{0.0012}

In Fig. 5 the α spectra obtained with the ^{241}Am α source for the different “sandwiches” are shown. All spectra were normalized to the total number of counts in the spectrum obtained with the 1.81 mg/cm^2 Ni-catcher (the data obtained with the worst statistics). The spectra were fitted with the Gaussian and NOLIN functions to obtain E_m and FWHM values. They are listed in Table I and compared to those obtained with TRIM simulations using the 5.486 MeV α -line spread additionally in accordance with the form of the α peak observed in the measurement without any degrader. The α spectra obtained with these simulations are shown in Fig. 6. In these simulations, the relative position of the source, “sandwich” and SSBD, as well as their dimensions, were taken into account.

The data listed in Table I and Figs. 5 and 6 indicate that the mean α -particle energies obtained in simulations with taking into account the form of α -line E_m^{TN} are very close to those obtained in the measurements. It means that the absorbed α -particle energy obtained in the simulations can give us a reliable estimate of an absorber thickness. In the case of α -radioactive ERs stopped inside a catcher foil, their mean α -particle energy obtained by the detection in backward direction can give us a reliable estimate of ER mean projected range R_m in the catcher. At the same time, the FWHM values of energy distributions obtained in the measurements and simulations are different from each other. The apparent reason of the difference might be the inhomogeneity of the catcher foils and targets, which was not taken into account in simulations and could not be simply obtained with the measurements. So, such derivation of the mean range values of heavy atoms could not be accompanied by any reliable estimates of their range straggling values σ_R . Note that the mean projected range for ^{203}Rn produced in the $^{194}\text{Pt}(^{16}\text{O}, 7n)$ at the beam energy of 125 MeV (the highest energy used in our beam experiments) is only 0.443 mg/cm^2 of Al, as calculated with SRIM. One could hope for the relatively small energy losses of α particles escaped from the Al catcher for the ERs collected by it. SRIM estimates range straggling in Al $\rho_{\text{Al}} \equiv \sigma_R/R_m = 9.1\%$ for ^{203}Rn that is significantly less than the one for Ni ($\rho_{\text{Ni}} = 15.9\%$). This preference for the Al catcher over the Ni one was kept in mind, since the range straggling could not be estimated in our α -particle transmission experiments.

B. Beam experiments

The main experiments on the measurement of the ER ranges were carried with the ^{16}O beam delivered by the XTU

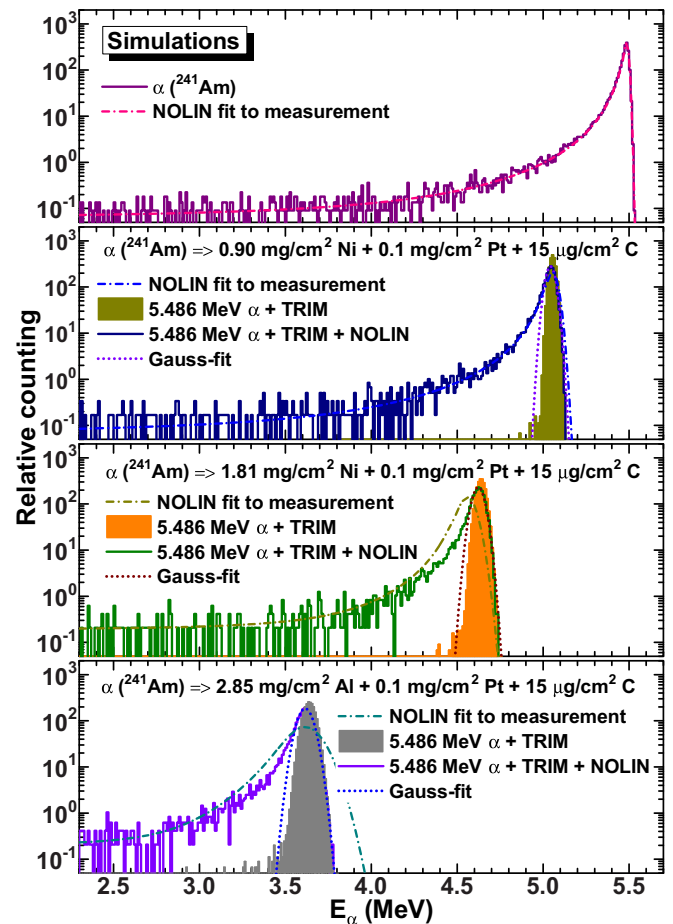


FIG. 6. The same as described in the caption of Fig. 5 but for the α spectra obtained with TRIM simulations using the mono-energy 5.486 MeV α line (filled Gaussian-like histograms) and for the similar ones accompanied by an additional spread according to the form of the α peak observed in the measurement without any degrader, as shown in the upper panel of Fig. 5 (histograms). The results of the NOLIN function fits shown in Fig. 5 are also shown for comparison (dash-dotted lines).

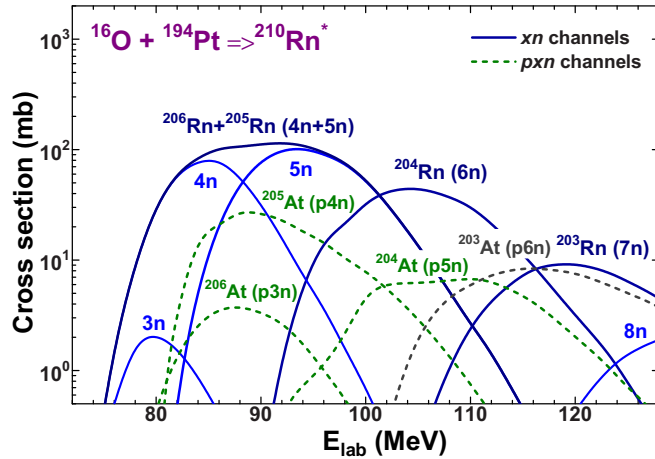


FIG. 7. The most probable evaporation channels in the $^{16}\text{O} + ^{194}\text{Pt}$ reaction, as obtained with the HIVAP calculations [25]. The excitation functions for the ERs that could be mainly detected according to their α -decay properties are shown by dark lines. See text for details.

Tandem accelerator of the Laboratori Nazionali di Legnaro of INFN. The ^{16}O beam energies $E_b = 80\text{--}125$ MeV and the intensities of 50–150 p nA were used in the irradiation of the Pt targets. Three 0.1 mg/cm^2 ^{194}Pt targets were placed on the ladder in the center of a scattering chamber having the diameter of 100 cm. They were evaporations of metallic ^{194}Pt on the $15\text{ }\mu\text{g/cm}^2$ carbon backing foils facing the beam. Isotopic enrichments of the targets were higher than 97%.

A rather limited number of the fusion-evaporation reactions with sufficient yields of ERs can be expected in the beam energy range used in our experiments. The most probable evaporation channels of the $^{16}\text{O} + ^{194}\text{Pt}$ reaction leading to the $^{210}\text{Rn}^*$ compound nucleus (CN) are shown in Fig. 7, as obtained with the statistical model calculations performed with the HIVAP code [25]. A lot of applications of HIVAP to the description of the production of non-fissile and fissile nuclei showed rather good reproducibility of measured excitation functions in the calculations [23,35,36]. As we can see in the figure, $^{206\text{--}203}\text{Rn}$ produced in the $4n\text{--}7n$ evaporation channels along with $^{206\text{--}203}\text{At}$ resulting from the $p3n\text{--}p6n$ evaporations are the most probable ERs that could be detected in our experiments. The At nuclei, evidently, could be also produced as the result of the EC decays of the Rn precursors.

The detection of the At and Po ERs produced in the pxn and αxn channels, respectively, is additionally limited by their small branches of α decay. The decay properties of ERs that could be detected in our experiments are listed in Table II [37]. As one can see, the most probable α -decay energies of Rn nuclei, as well as their α branches, substantially exceed those for the At ones having the same mass numbers. The only At nucleus, whose production rate could be compatible with the one for ^{203}Rn , is ^{203}At produced in the $p6n$ reaction. Fortunately its α -decay energy differs essentially from the one for ^{203}Rn . Close α -decay energies of ^{206}Rn and ^{205}Rn produced in the $4n$ and $5n$ evaporation channels, respectively, could not be clearly resolved in our experiments which implied only

TABLE II. The α -decay properties of Rn and At nuclei produced in the $^{16}\text{O} + ^{194}\text{Pt}$ reaction. The most probable α -decay energies E_α and their α branches are indicated [37].

Nucleus	E_α (MeV)	α branch (%)	Half-life (s)
^{207}Rn	6.131	21	555
^{207}At	5.758	8.6	6480
^{206}Rn	6.260	63	342
^{206}At	5.703	0.86	1836
^{205}Rn	6.261	24.2	170
^{205}At	5.902	10	1614
^{204}Rn	6.417	72.4	74.5
^{204}At	5.950	3.91	547
^{203g}Rn	6.499	64	44
^{203m}Rn	6.550	75	26.9
^{203}At	6.087	27	444
^{202}Rn	6.640	78	9.85

crude measurements of the decay curves for the observed α activities.

We used the arrangements schematically shown in Fig. 8. A sketch shown in Fig. 8(a) corresponds to the experiments

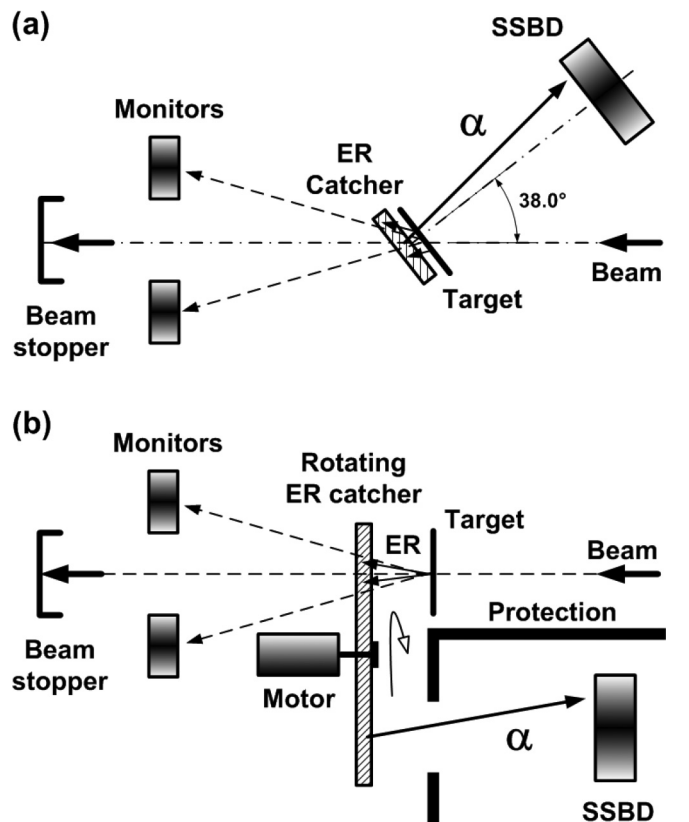


FIG. 8. Schematic view on the configuration of the detection of α -decays from ERs produced in the $^{16}\text{O} + ^{194}\text{Pt}$ reaction. (a) ERs were collected by a stationary catcher foil with the detection of α -particles at a backward angle in the regime of “ER collection– α detection.” (b) ERs were continuously collected and delivered to the detector located in the protected area with a rotating catcher foil installed nearby the target.

performed with a stationary catcher foil in the regime of “ERs collection— α detection,” when the beam was switched-on and switched-off within 10 min in duration. This regime allowed one to collect and detect effectively α -radioactive Rn nuclei with half-life $1 \lesssim T_{1/2} \lesssim 5$ min. One of the ^{194}Pt target coupled with the catcher foil was installed at the fixed angle to the beam direction that allowed one to reduce the energy losses of α -particles escaped at about right angle to the catcher plain in the direction to the SSBD. A solid angle subtended by the SSBD placed at 6.5 cm away from the target-catcher position at a backward angle to the beam was $\sim 0.8\%$ for α particles emitted within 4π .

Figure 8(b) corresponds to the majority of experiments performed with the Al rotating catcher installed behind and nearby the target. ERs were continuously collected and delivered to the protected area, where α -particles from the ER decays were detected by the SSBD installed at about the same distance from the catcher plane as in the experiments with the stationary catcher. About the same detection efficiency, as in the previous case, was provided for the α particles of ERs caught by the rotating catcher and delivered to the position in front of the SSBD. In the experiments, the condition for rotation time $T_{\text{rot}} \ll T_{1/2}$ was fulfilled for ERs produced in our experiments, that is, the losses of Rn ERs due to their decays during transportation to the SSBD were negligible.

The examples of the α -spectra recorded for the experiments corresponding to both the configurations are shown in Fig. 9. Each run was carried out at the beam energy $E_b = 100$ MeV with the 2.85 mg/cm^2 Al catcher foil. Fig. 9(a) presents the α -spectrum obtained in the run with six successive cycles of the “collection–detection” in the configuration (a), whereas Fig. 9(b) shows a similar spectrum recorded in the configuration (b) with the rotating catcher. The ERs produced in the reaction [indicated in Fig. 9(a)] were identified according to the energies of α particles and roughly measured decay curves obtained just after the end of each run.

As one can see in Fig. 9(a), positions of maxima for α peaks are shifted to lower energies by ~ 0.3 MeV relatively to the values tabulated for the nuclei indicated in the figure (see Table II). These shifts are indicated by the left and right vertical arrows for the observed and tabulated energies, respectively, and connected by horizontal lines in the figure. In the case of the rotating catcher the energy losses of α particles are somewhat greater [see Fig. 9(b)] because of their longer path inside the catcher. Nevertheless, the widths of peaks allow one to resolve the neighbor α peaks assigned to ^{205}Rn and ^{204}Rn having the original α energies of 6.261 and 6.417 MeV, respectively, with the use of a standard LSM-procedure for the Gaussian form of α peaks. Note that the width of α peaks observed with the rotating catcher (FWHM = 136 keV) is somewhat greater than a similar one obtained with the stationary catcher (FWHM = 122 keV). Nevertheless, both values are lower than a similar one estimated from α spectra obtained for Rn ERs produced in the $^9\text{Be} + ^{208}\text{Pb}$ reaction in the experiments with a pulsed beam and an annular SSBD (FWHM $\simeq 170$ keV) [33]. Note that the calculates ranges for the 2 MeV ERs [5] produced in this reaction are two times smaller than those produced in $^{16}\text{O} + ^{194}\text{Pt}$. At the same time, FWHMs for α peaks obtained in our experiments are

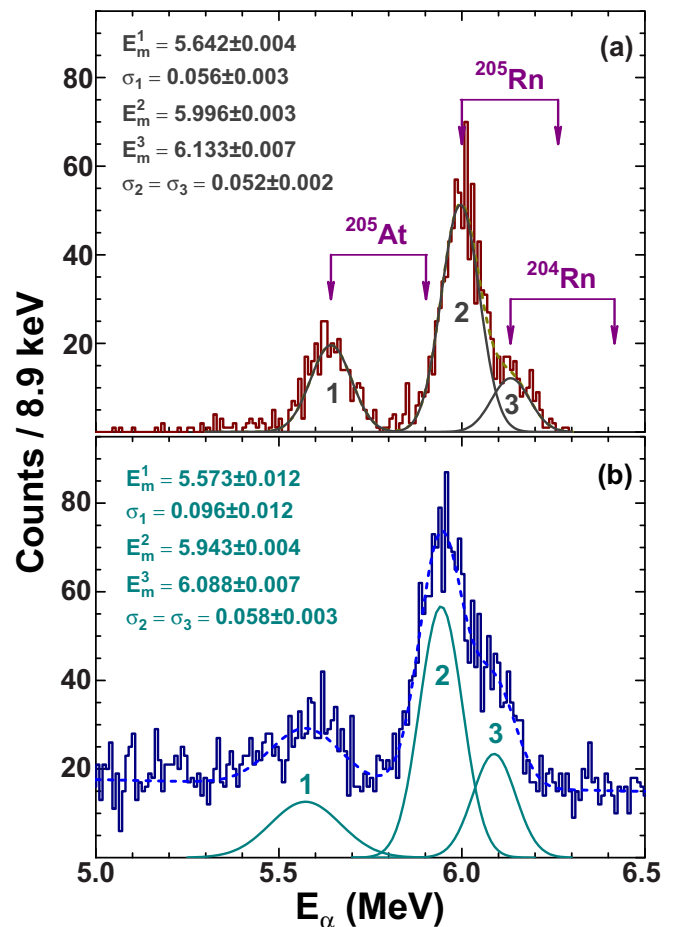


FIG. 9. The examples of α -spectra collected for two different $^{16}\text{O} + ^{194}\text{Pt}$ runs at beam energy $E_b = 100$ MeV. In both cases ERs were collected by 2.85 mg/cm^2 Al catcher foil: (a) installed stationary just behind the target, as shown in Fig. 8(a); and (b) rotating in a plane parallel to the target plane and located at some distance from the target, as shown in Fig. 8(b). The results of fits with three Gaussians are indicated for both spectra. See details in the text.

comparable with those obtained in the $^{12}\text{C} + ^{209}\text{Bi}$ catcher experiments using the off-line α -particles detection [38].

The applicability of the catcher techniques considered above is limited by the life time of produced nuclei. A scheme like the one shown in Fig. 8(a) is suitable for the detection of α -activities with $T_{1/2} \gtrsim 1$ min, when off-line measurements are impossible. A scheme with the rotating catcher can be applied to the detection of ERs with $T_{1/2} \gtrsim 1$ ms. One more limitation in the use of these techniques is a low geometrical efficiency for the detection of α particles, which has to be accepted to obtain a better resolution. The efficiency can be increased up to $\sim 5\%$ without significant losses in the resolution as shown by TRIM simulations. In the case of the rotating catcher, a higher detection efficiency can be achieved with a number of detectors installed at the periphery of the catcher disk. In our case of the Rn ranges deduced with these techniques, experiments with the Al rotating catcher were preferable due to the direct comparison of the reduced α -particle energies with those obtained using TRIM simulations.

The rotating catcher experiments provide more effective beam time consumption as compared to those using the stationary catcher. Nevertheless, several experiments with the latter were also carried out, since they provided better background conditions ensuring an additional confirmation in the assignment of the observed α -particle energies. The most intensive α peaks observed in the experiments were only analyzed to reduce the errors in the derived Rn ranges.

III. SIMULATIONS AND DATA ANALYSIS

Simulations of α spectra, to be compared with the measured ones, were performed for ERs spread out over the catcher plane. The energy and angular distributions of ERs knocked out from the target were initially simulated to obtain the ER range distributions. The spreads in the ER energy and angular distributions are determined by the evaporation of light particles (neutrons) from the $^{210}\text{Rn}^*$ CN, as well as by their energy losses and multiple scattering inside the target. The last two processes are interconnected and can be considered using TRIM simulations. In these simulations we assumed a uniform production of ERs along the target thickness, which is a good approximation for relatively thin targets providing small projectile energy losses. The initial energy and angular distributions for ERs produced inside the target were randomly simulated using mean energies of the evaporated particles at each step of the CN de-excitation chain leading to the observed ER. These energies were obtained with the statistical model calculations [25]. The sequential computation of the velocity vectors for the evaporated particles and heavy nuclei produced at each evaporation step allowed to take into account charged particles emission (protons and α 's) at the CN de-excitation along with the emission of neutrons. This approach extended the description of the energy and angular distributions, which was earlier applied to the reactions with evaporation of neutrons [23].

The example of the ^{206}Rn spatial distribution over the rotating catcher area, as obtained with such simulations at the 84 MeV beam energy, is shown in Fig. 10. Due to the proximity of the catcher foil to the target, almost all ERs knocked out from the target were implanted into the foil. The geometry of the SSBD, protecting diaphragm [see dimensions in Fig. 10(a)] and the distance from the catcher to the SSBD allowed one to “view” 17.1% of ERs collected by the catcher. The α spectra collected for the run at this beam energy are shown in Fig. 11(a). A single peak was observed in the on-line measurement with the beam, as well as in the further exposition just after stopping the beam for a measuring time t_m [see insert in Fig. 11(a)]. ^{206}Rn is the most probable ER that can be produced at this energy, as it followed from the calculations [25] (see Fig. 7) and from our rough decay-curve measurement. The ^{206}Rn range distribution and α spectra corresponding to different ranges in Al for the 6.260 MeV α -source, which were obtained with simulations, are shown in Fig. 11(b). As one can see, maxima of α energies E_m^i obtained with the Gaussian fits to the simulations (see Sec. II A) are successively approached to the E_m value obtained in the measurements [Fig. 11(a)], as the Rn range increases. Increasing the range was realized by adding a con-

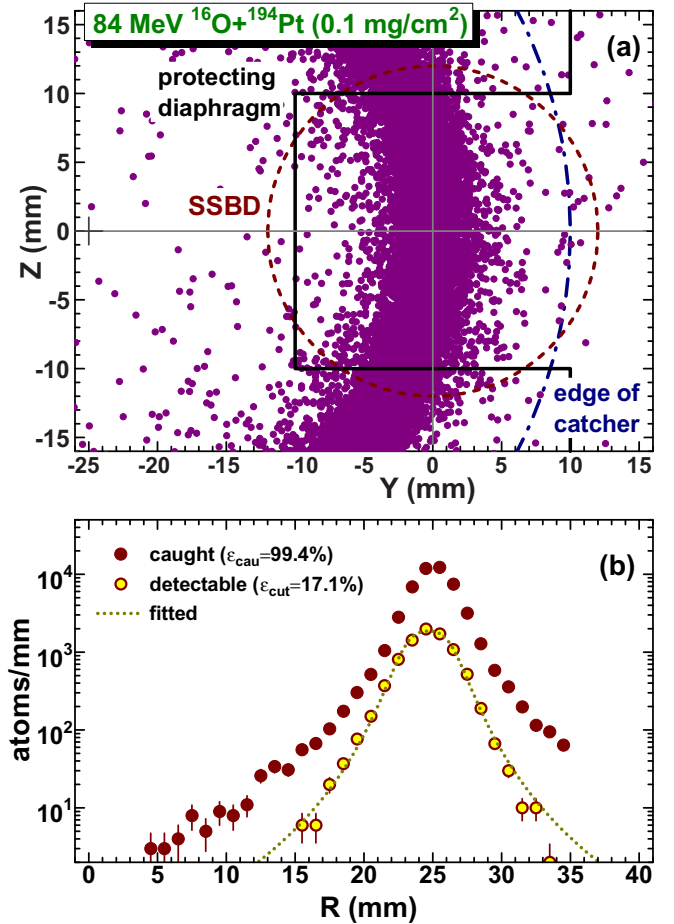


FIG. 10. (a) ^{206}Rn distribution over the catcher plane (dots), as obtained with the simulation at beam energy $E_b = 84$ MeV. A geometry in the plane of the rotating catcher, protecting diaphragm and SSBD (different lines) is shown for orientation. The events that fall on the diaphragm area and out of edge of the catcher could not be detected by SSBD. (b) ^{206}Rn radial distributions (atoms/mm) for ERs caught by the catcher (full circles) and for those that could pass through the window of the protecting diaphragm and whose α -particles could be detected (open circles). The latter was fitted by the inverse polynomial function (dotted line). See details in the text.

stant to the simulated ranges, which was expressed through mean value R_m corresponding to the original TRIM simulation [see insert in Fig. 11(b)]. A linear fit to the E_m^i values as a function of mean ranges R_i , which are shown in Fig. 11(b) for $i = 1-3$, and the use of E_m resulting from the analysis of the measured α spectra, allowed one to estimate the mean range value expressed through relative value $(R_m/R_m^{\text{TRIM}})_{\text{est}}$. The example of such estimate of the ^{206}Rn mean range in Al is shown in Fig. 12 for the data presented in Fig. 11.

In Sec. IV the approach described above will be applied to the analysis of α spectra obtained at beam energies $E_b = 80, 88, 92, 96, 100, 105, 110, 115, 120,$ and 125 MeV. As mentioned above the most intensive high-energy α peaks corresponding to the production of Rn nuclei were used for the estimates of Rn ranges. In this respect we dealt with the α spectra similar to the one shown in Fig. 11(a) at the beam

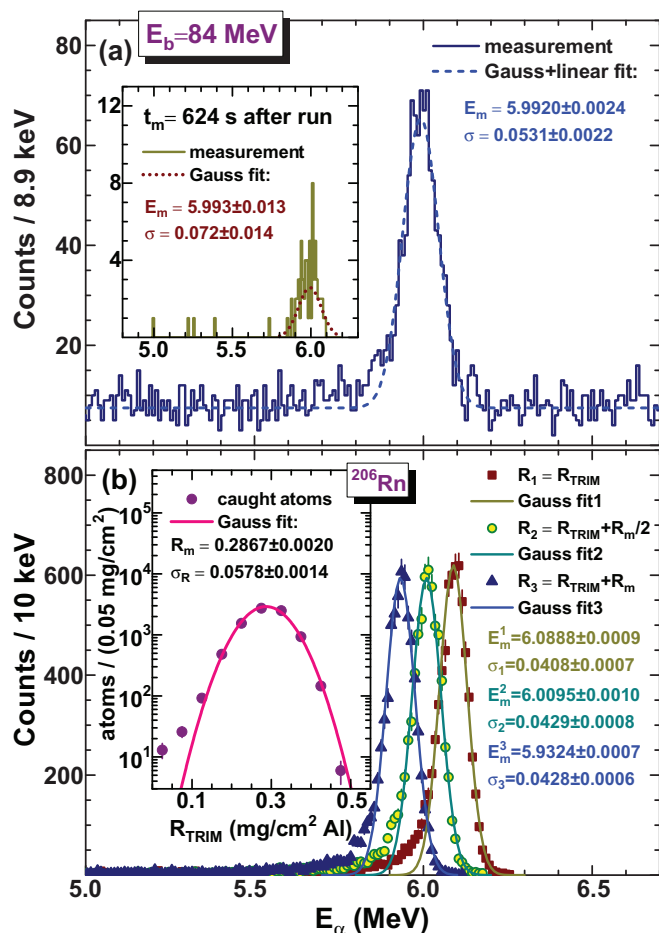


FIG. 11. (a) The α spectrum collected on-line with the Al rotating catcher at $E_b = 84$ MeV (histogram) and the one obtained for 624 s just after the run (insert) together with Gaussian fits to the observed α peaks (dashed lines). (b) α -spectra simulated for the 6.260 MeV α source distributed over a depth in Al according to the different ^{206}Rn ranges R_i . The original ^{206}Rn range distribution in Al, as obtained with the TRIM simulation, is shown in the insert. Gaussian fits to the range and α -spectrum simulations are shown by solid lines.

energies of 80 to 96 MeV. These spectra reflected the production of $^{206,205}\text{Rn}$. At $E_b = 100$ MeV the ^{204}Rn production was observed according to the resolved high-energy α peak spaced by $\simeq 150$ keV from the main peak assigned to ^{205}Rn (see Fig. 9). The α spectra observed at higher beam energies are shown in Fig. 13. At $E_b = 105$ and 110 MeV the α peak of ^{204}Rn dominates over the one assigned to ^{205}Rn . The latter completely disappears at 115 MeV, whereas the α peak assigned to ^{203g}Rn appears, whose energy is reduced to about 6.14 MeV (see Fig. 13). It is shifted to low energies by nearly the same value as the peak of ^{204}Rn . At $E_b = 120$ MeV the yields of ^{204}Rn and ^{203g}Rn are comparable, whereas at the highest energy $E_b = 125$ MeV the relative yield of ^{203g}Rn dominates. The decomposition of the observed α spectra was performed with the fits of 3 or 4 Gaussians, assuming the presence of a linear background in the region of 5 to 7 MeV, as shown in Fig. 13. Note that variations in the yields of the observed α activities with the beam energy, as they were

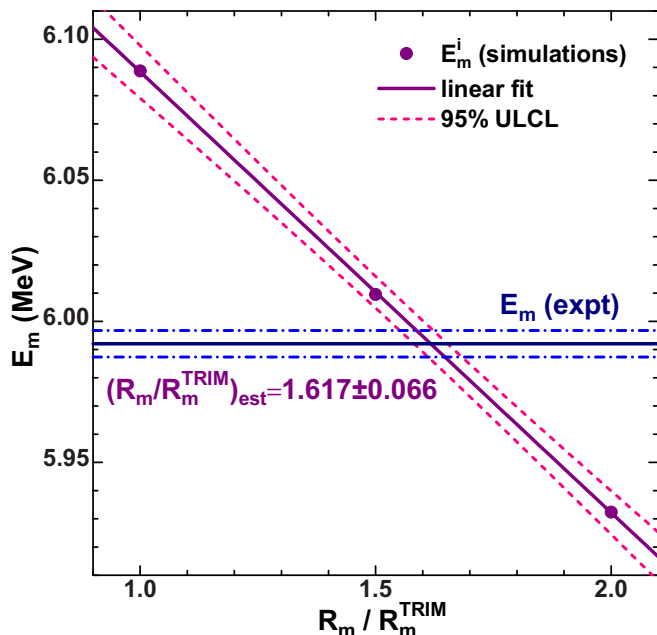


FIG. 12. The estimate of the relative value of $(R_m/R_m^{\text{TRIM}})_{\text{est}}$ using the mean value of the α -particle energy E_m obtained in the experiment [see Fig. 11(a)] and a linear fit to the E_m^i values obtained in simulations (full circles), which are displayed as a function of mean ranges R_i [see Fig. 11(b)]. The E_m value, as the result of the Gaussian fit to the observed α peak is shown by a horizontal solid line accompanied by dash-dotted lines corresponding to the 95% confidence limit. The results of the linear fit are shown by a slanted solid line accompanied by dashed lines corresponding to the same confidence limit.

extracted with our fits, are in accordance to the excitation functions for the production of Rn isotopes (see Fig. 7) and their α -branching ratios (see Table II).

IV. RESULTS AND DISCUSSION

The results of our study of the ranges in Al of Rn ERs produced in the $^{16}\text{O} + ^{194}\text{Pt}$ reaction are listed in Table III. The ranges are given for beam energies E_b and for mass number A of isotopes having the highest yields. In the table the ranges predicted by SRIM R_{SRIM} at energy calculated as $E_{\text{ER}} = E_b A_p A_{\text{ER}} / (A_p + A_t)^2$ (see notations in Sec. I) are presented for reference. We also present the Rn mean energies E_m^{sim} and standard deviations σ_E^{sim} , as the quantities that characterized the input energy distributions. We note that these values characterize those ERs that could be caught by the catcher and detected by the SSBD [see Fig 10(b)]. As we mentioned in Sec. III, the initial energy and angular distributions for ERs produced inside the target, which are determined by the evaporation of light particles, were simulated using mean energies of the evaporated particles. The input energy distributions were obtained with MC simulations, assuming the uniform production of ERs along the target thickness and taking into account small projectile energy losses inside the carbon backing and target. In the table, we also present the quantities that characterize the range distributions of Rn

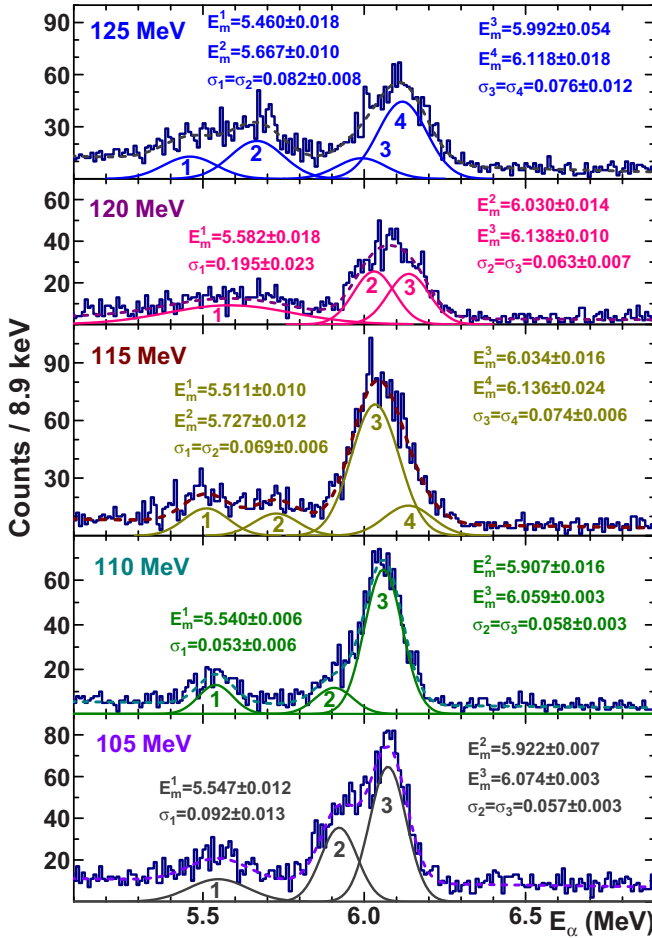


FIG. 13. The α spectra obtained at beam energies $E_b = 105, 110, 115, 120,$ and 125 MeV (histograms) in experiments with the Al rotating catcher. The results of the model fits to the spectra are shown by dashed lines. A fitting model used the 3 or 4 Gaussians and a linear background. The α peaks extracted with the fits are shown by solid lines. The main parameters resulting from the fits are indicated in each panel corresponding to the specified beam energy.

isotopes according to TRIM simulations R_m^{TRIM} and σ_R . They correspond to input energy and angular distributions [see the example in Fig. 11(b)]. In the last column we list relative values of excess in the mean ranges $(R_m/R_m^{\text{TRIM}})_{\text{est}}$, as estimated from the comparison of the mean α -particle energies obtained in the measurements and of those obtained in our simulations of the ranges and α -particle energies (see the example in Fig. 12).

As one can see in Table III, Rn ranges obtained in our experiments significantly exceed those that could be expected from SRIM/TRIM calculations/simulations. This excess is displayed in Fig. 14 and it corresponds to mean value $(R_m/R_m^{\text{TRIM}})_{\text{est}} = 1.650 \pm 0.011$ (a standard error). The value derived is higher than the similar one obtained for the ranges of Po, At, and Ac ERs produced in the $^{16,18}\text{O}+\text{Ir}$ and $^{12}\text{C}+\text{Bi}$ reactions. For these ERs the excess over SRIM ranges is estimated by a factor of 1.3–1.4 at the same energies (see Fig. 4). As we mentioned in Sec. I, the reason of such excesses might be lower values of the stopping power (namely, its

components, the electronic and/or nuclear ones) than it is implied in SRIM/TRIM calculations/simulations (see Fig. 1, as an example). In this connection it was of interest to check the ability of the empirical parametrization of the Al stopping power for HIs [3] to reproduce the ranges of low-energy heavy atoms such as Rn.

Figure 15 shows the relative values of HI effective charges γ in Al, which have been derived in Ref. [3] from the measured SP data [29]. In the figure the low energy part of the plot (see Fig. 11 in Ref. [3]) with the similar approximation mentioned in Sec. I is displayed in a linear V_{red} scale. At $V_{\text{red}} \leq 0.14$ a linear approximation to the data is used. With the integration of empirical SP values SP_{emp} corresponding to the linear approximation of γ -values one could obtain the ranges of Rn as $\int_0^{E_0} dE/SP_{\text{emp}}$ (E_0 is the input energy). These ranges turned out to be higher than those obtained in our experiments by a factor of about two. We note that the contributions of the nuclear stopping SP_n to the measured SP values were ignored (not subtracted from the measured values) in the parametrization [3]. This contribution according to the SRIM prediction is shown in Fig. 15 for ^{127}I (the heaviest low energy ion for which Al SP data were obtained) and for ^{205}Rn of present interest. As one can see in the figure, nuclear stopping is the main factor determining the HI energy losses at the end of their ranges in matter.

We attempted to take into account nuclear stopping for the Rn ranges estimated with the use of the empirical approach [3] and using nuclear stopping powers given by SRIM SP_n^{SRIM} . The results are shown in Fig. 16 for the SP_n^{SRIM} values reduced by 30%. With electronic stopping powers providing by SRIM SP_e^{SRIM} a similar agreement with the data could be obtained using SP_n^{SRIM} values reduced by 70%. In both cases the ranges were calculated as $\int_0^{E_0} dE/(SP + kSP_n^{\text{SRIM}})$, where $SP = SP_{\text{emp}}$ or SP_e^{SRIM} and k is an adjusted parameter. As we can see again in the figure, the nominal SRIM/TRIM calculations/simulations underestimate the Rn range data obtained in the present work. However, the reduced values of the nuclear stopping power given by SRIM together with the empirical values of SP_{emp} or the electronic SP_e^{SRIM} allowed us to reproduce the Rn ranges almost in the same way as it can be obtained with the aE^b function fit. Note that total SRIM SPs at $V_{\text{red}} > 0.2$ are in general agreement with the experimental data and are very close to SPs obtained with the empirical γ approximation, as one can see in Fig. 15. So, one could come to the conclusion that both the components of SRIM SPs should be reduced to obtain the agreement of the predictions with the experimental data for heavy atoms at low energies.

The question arises of whether the excess in the Rn ranges over the values predicted by different ways is inherent in Rn atoms, bearing in mind their shell structure, or it is a general feature in stopping of low energy heavy atoms, bearing in mind earlier observations reported in References [6,8,10,22]. One should note that in experiments we usually deal with accelerated heavy ions charged to a definite charge state which is far from the HI equilibrated charge state in matter. The charge states evolve with the penetration of HI into a stopping medium, as deduced from classical trajectory Monte Carlo

TABLE III. The results of the study of the ranges in Al for Rn isotopes produced in the fusion-evaporation $^{16}\text{O} + ^{194}\text{Pt}$ reaction for ^{16}O beam energies E_b and isotopes with atomic mass number A . Ranges predicted by SRIM R_{SRIM} for Rn energies E_{ER} (see the text for explanation) are presented for reference. Rn mean energies E_m^{sim} and their standard deviations σ_E^{sim} obtained in simulations (see the text for details), as well as the quantities characterizing the input energy distributions and the resulting quantities R_m^{TRIM} and σ_R are also presented. In the last column the relative values of excess in mean ranges $(R_m/R_m^{\text{TRIM}})_{\text{est}}$, as estimated from the comparison of the mean α -particle energies obtained in the measurements and of those obtained in our simulations for the ranges and α -particle energies. The error corresponding to the 95% confidence level are indicated as subscripts and superscripts for the $(R_m/R_m^{\text{TRIM}})_{\text{est}}$ values.

E_b (MeV)	A	E_{ER} (MeV)	R_{SRIM} (mg/cm ²)	E_m^{sim} (MeV)	σ_E^{sim} (MeV)	R_m^{TRIM} (mg/cm ²)	σ_R^{TRIM} (mg/cm ²)	$(R_m/R_m^{\text{TRIM}})_{\text{est}}$
80	206	5.979	0.289	5.665	0.752	0.272	0.0550	$1.668^{+0.045}_{-0.045}$
84	206	6.278	0.303	6.007	0.733	0.287	0.0578	$1.617^{+0.066}_{-0.066}$
88	206	6.577	0.319	6.282	0.772	0.300	0.0595	$1.631^{+0.032}_{-0.033}$
	205	6.545	0.316	6.258	0.773	0.299	0.0600	
92	205	6.843	0.330	6.549	0.840	0.312	0.0623	$1.551^{+0.079}_{-0.080}$
96	205	7.140	0.346	6.859	0.858	0.327	0.0651	$1.615^{+0.073}_{-0.067}$
100	205	7.438	0.359	7.155	0.888	0.341	0.0658	$1.647^{+0.064}_{-0.061}$
	204	7.401	0.357	7.130	0.888	0.340	0.0673	$1.749^{+0.094}_{-0.090}$
105	205	7.810	0.376	7.525	0.919	0.359	0.0692	$1.706^{+0.152}_{-0.132}$
	204	7.771	0.376	7.500	0.938	0.357	0.0701	$1.732^{+0.088}_{-0.079}$
110	204	8.142	0.392	7.898	0.984	0.376	0.0721	$1.691^{+0.035}_{-0.035}$
115	204	8.512	0.411	8.263	1.024	0.392	0.0743	$1.741^{+0.172}_{-0.164}$
120	204	8.882	0.427	8.640	1.081	0.409	0.0770	$1.678^{+0.249}_{-0.207}$
	203	8.838	0.424	8.604	1.095	0.407	0.0772	$1.591^{+0.110}_{-0.108}$
125	203	9.206	0.443	8.965	1.164	0.425	0.0814	$1.609^{+0.198}_{-0.194}$

simulations taking into account the interaction of all target and projectile electrons along the ion path [39]. Close to the surface, HI energy losses also strongly changing with the depth of penetration and may also evolve depending on different incoming charge states [39]. When entering the solid, a projectile loses or picks up electrons until it reaches the

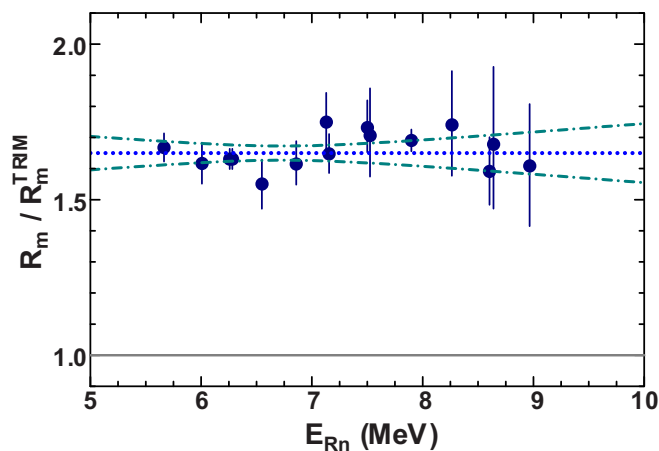


FIG. 14. The relative excess in the mean Rn ranges in Al over similar values that can be obtained with TRIM simulations, as derived from the present work (see Table III). The mean value of the excess obtained with a constant fit to the data is shown by a dotted line accompanied by dash-dotted lines corresponding to the 95% confidence level.

equilibrated charge state within a definite path length, in accordance with the experimental observations [40]. As for

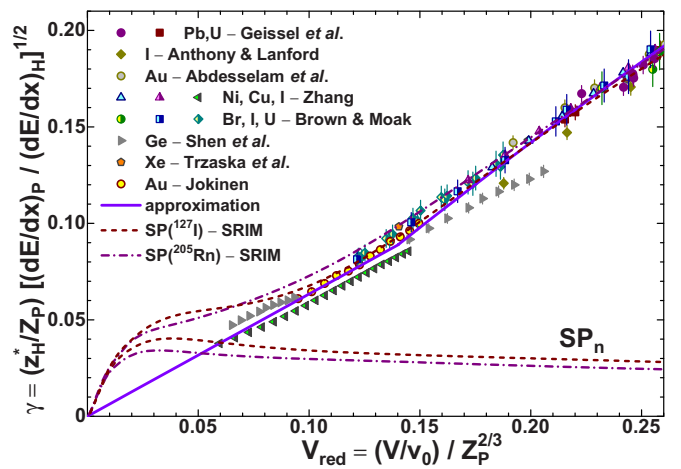


FIG. 15. The relative values of HI effective charges γ in Al, as derived from the measured SP values [29] (different symbols). The low-energy part of the plot (see Fig. 11 in [3]) and similar approximation as mentioned in Sec. I are displayed in a linear V_{red} scale. The fitted curve resulting from the two-parameter function fit to the data at $V_{\text{red}} \geq 0.14$ and the linear approximation at $V_{\text{red}} \leq 0.14$ are shown by the solid line. Total stopping powers (SP) and their nuclear components SP_n obtained according to SRIM predictions and converted to the corresponding γ values for ^{127}I and ^{205}Rn are shown by dashed and dash-dotted lines, respectively. See details in the text.

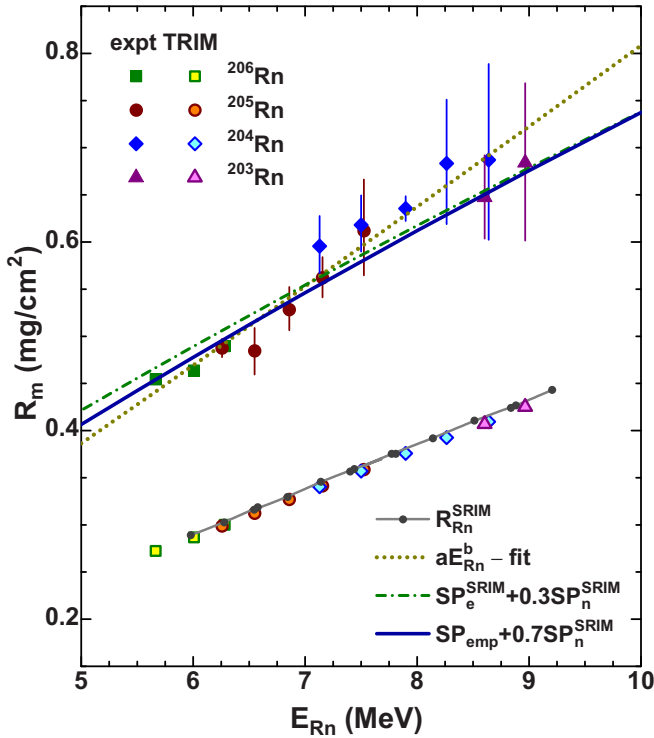


FIG. 16. The mean ranges of Rn isotopes in Al, as deduced from the present work (different full symbols) in comparison with the corresponding values obtained with SRIM calculations and TRIM simulations (dots connected with a solid line and open symbols, respectively). These data are also listed in Table III. The ranges obtained with the aE_{Rn}^b function fit and with the use of electronic stopping power given by SRIM SP_e^{SRIM} and by empirical SP values SP_{emp} together with the variation of nuclear stopping power given by SRIM SP_n^{SRIM} are shown by different lines. For the last two cases the calculated ranges shown by dash-dotted and solid lines correspond to the best agreement with experimental data.

the recoiled ERs produced in fusion-evaporation reactions, they have a very broad spectrum of charge states consisting of the equilibrated component and nonequilibrated one, which have poorly predictable relationship between them [41]. This adds complexity to the interpretation of such experimental data. In this context it should be noted that the SRIM/TRIM energy losses or range calculations/simulations completely ignore the input charge state of HIs, but they deal with the equilibrated charges inside media. As a result, most of these calculations/simulations give quite acceptable results (in agreement with experimental data), since the HI charge state is energy dependent, and the incoming HI may take quite a while to reach the equilibrated state.

V. SUMMARY AND CONCLUSION

The energy losses of low-energy heavy ions (HIs) in solids are reasonably well reproduced with the Monte Carlo (MC) TRIM simulations [the most popular code for the estimates of HI stopping powers (SPs) and ranges in matter] [5]. That is the case for the projectiles with the atomic number $Z_P \leq 62$,

which have passed through a carbon foil and were detected in forward direction [2,3]. The angle selection allows one to reduce significantly the effect of the nuclear stopping power (SP_n) component, which along with the electronic one (SP_e), determines HI energy losses in matter at low energies. However, the results of TRIM simulations show a considerable excess over the experimental data obtained for the HI energy losses of four heavier projectiles with $Z_P > 62$ [2]. A presence of so-called Z_P -oscillations observed for SPs of projectiles with $Z_P \leq 40$ are also reproduced in the same TRIM simulations as well as in SRIM calculations (but with an excess in SPs over the experimental data) (see Fig. 1). The extension of the number of projectiles with $Z_P > 62$, for which SPs could be measured seems to be desirable for clarifying the problem of stopping of low energy heavy atoms.

Manifestation of Z_P oscillations and contributions of the SP_e and SP_n components could be considered in the analysis of the ranges of heavy atoms in light stopping media. The bulk of the range data in Al was obtained for radioactive evaporation residues (ERs) produced in fusion-evaporation reactions induced by HIs [11–22,24]. Comparison of the data for Ba, Sm, Tb, and Dy ERs [11–16] with the results of SRIM calculations shows about 10% overestimate for the Ba and Sm calculated ranges and the same underestimate for the Tb and Dy calculated ranges at energies less than 0.1 MeV/u compared to the experimental data (see Fig. 2). Unfortunately, for heavier ERs (from Hf to Tl), irregular data which are inconsistent with each other are available [17–20,24]. At the same time, for heavier ERs (Po, At and Ac) [13,21,22] the ranges reveal a 30–40% excess over the calculated ranges at energies below 0.05 MeV/u (see Fig. 4).

Correct range values for heavy ERs are necessary for establishing the mechanism(s) of their production in incomplete fusion (multinucleon transfer) reactions. As one could expect and it was shown with different model calculations and measurements for heavy (targetlike) reaction products, their recoil energies and corresponding ranges differ noticeably from those that are inherent in ERs produced in complete fusion reactions [17–20,22,24,30–32]. So, extending an available bulk of the range data for heavy ERs is of direct interest from different points of view.

The ranges of the short-lived Rn isotopes in Al, which were produced in the $^{16}\text{O} + ^{194}\text{Pt}$ fusion-evaporation reaction, have been obtained for the first time. Rn isotopes knocked out from the Pt target by the ^{16}O beam with energies from 80 to 125 MeV were implanted into a rotating Al catcher delivering continuously α -radioactive nuclei produced in the reaction to a semi-conductor surface-barrier detector (SSBD). The SSBD was facing the catcher plane and placed in the protected area. The α -particle energies of nuclei collected by the catcher, which escaped from the catcher in opposite direction to the beam, were continuously detected in each run. These energies were reduced by ~ 0.3 MeV due to the definite ranges of Rn isotopes stopped in the catcher. The exact energy corresponding to the observed α -peak maximum(s) E_m was determined by fitting of the Gaussian(s) to the observed α peak(s). This energy was compared with the one obtained in simulations.

First, the range distribution was simulated for the Rn isotope most probably produced in the neutron evaporation reaction at the beam energy under study. The initial angular and energy distributions of Rn ERs determined by evaporation of neutrons and their stopping inside the Pt target were taken into account. The geometry of their collection and the detection of the emitted α particles by the SSBD were also taken into account. Stopping of Rn atoms inside the target and their initial range distribution in Al were obtained with TRIM simulations. Thus, the obtained Rn range distribution inside the catcher foil was used for the TRIM simulations of the energies of α particles escaping from the catcher. These energies were corrected for the form of the α peak, previously obtained in the measurements with the ^{241}Am α source. Resulting mean α -particle energy E_m was obtained with the Gaussian fit to the simulated α peak. For all cases corresponding to the beam energies under study, the simulated Rn ranges were insufficient to reproduce the mean α -particle energies observed in the experiments, i.e., the E_m values obtained in simulations were remarkably higher than those obtained in the experiments. The Rn ranges were resimulated with increased values of the ranges using the step corresponding to $0.5R_m$, where R_m is the mean value obtained with the Gaussian fit to the initial range distribution. With two additional simulations thus performed a linear dependence $E_m(R_m)$ was obtained, whose intersection with the horizontal line corresponding to the E_m energy obtained in the experiment allowed us to estimate the experimental value of R_m .

As the result of this procedure applied to the 15 points of the beam energy, which corresponded to the production

of the ^{206}Rn to ^{203}Rn ERs in the neutron evaporation reactions, the ranges obtained in our experiments significantly exceeded those that could be expected from SRIM/TRIM calculations/simulations. This excess corresponds to mean value $(R_m/R_m^{\text{TRIM}})_{\text{est}} = 1.650 \pm 0.011$. This value is higher than a similar one obtained for the ranges of Po, At, and Ac ERs produced in the $^{16,18}\text{O}+\text{Ir}$ and $^{12}\text{C}+\text{Bi}$ reactions, for which the excess over SRIM ranges is expressed by a factor of 1.3–1.4 at the same ER energies.

In an attempt to achieve an agreement with the experiments, lower nuclear stopping powers than it is used in SRIM calculations were tested for the calculated Rn ranges. Thus, in the case of the use of the stopping power (SP) given by SRIM, its nuclear component SP_n^{SRIM} has to be reduced by 70% to reproduce the Rn ranges obtained in the experiments. In the case of SP corresponding to the effective charge parametrization of the experimental SP values obtained at low energies, the 30% reduction of the nominal SP_n^{SRIM} values allows one to reproduce the Rn ranges. So, one could come to the conclusion that both the components of SP should be reduced to obtain an agreement of the predictions with the experimental data for the ranges of heavy atoms at low energies.

ACKNOWLEDGMENTS

We thank the XTU Tandem staff for their careful work allowing us to carry out the beam experiments and Drs. P. Mason and R. Silvestri for their participation in some measurements.

-
- [1] P. Hvelplund and B. Fastrup, *Phys. Rev.* **165**, 408 (1968).
 - [2] W. N. Lennard, H. Geissel, D. P. Jackson, and D. Phillips, *Nucl. Instrum. Methods Phys. Res., Sect. B* **13**, 127 (1986).
 - [3] R. N. Sagaidak, V. K. Utyonkov, and S. N. Dmitriev, *Nucl. Instrum. Methods Phys. Res., Sect. B* **365**, 447 (2015).
 - [4] D. Ward, H. R. Andrews, I. V. Mitchell, W. N. Lennard, R. B. Walker, and N. Rud, *Can. J. Phys.* **57**, 645 (1979).
 - [5] J. F. Ziegler, code SRIM, <http://www.srim.org>
 - [6] Y. Zhang, *Nucl. Instrum. Methods Phys. Res., Sect. B* **196**, 1 (2002).
 - [7] K. Jin, Y. Zhang, Z. Zhu, D. A. Grove, H. Xue, J. Xue, and W. J. Weber, *J. Appl. Phys.* **115**, 044903 (2014).
 - [8] H. Paul, in *Application of Accelerators in Research and Industry*, edited by F. D. McDaniel, B. L. Doyle, G. A. Glass, and Y. Wang, *AIP Conf. Proc.* **1525**, 309 (2013).
 - [9] L. G. Glazov and P. Sigmund, *Nucl. Instrum. Methods Phys. Res., Sect. B* **207**, 240 (2003).
 - [10] M. Behara, P. F. P. Fichtner, P. L. Grande, and F. C. Zawislak, *Mater. Sci. Eng., R* **15**, 1 (1995).
 - [11] M. Kaplan and J. L. Richards, *Phys. Rev.* **145**, 153 (1966).
 - [12] M. Kaplan and R. D. Fink, *Phys. Rev.* **134**, B30 (1964).
 - [13] L. Winsberg and J. M. Alexander, *Phys. Rev.* **121**, 518 (1961).
 - [14] J. M. Alexander and D. H. Sisson, *Phys. Rev.* **128**, 2288 (1962).
 - [15] G. N. Simonoff and J. M. Alexander, *Phys. Rev.* **133**, B104 (1964).
 - [16] J. B. Natowitz and J. M. Alexander, *Phys. Rev.* **188**, 1734 (1969).
 - [17] E. Gadioli, *Acta Phys. Pol. B* **30**, 1493 (1999).
 - [18] M. K. Sharma, Unnati, B. K. Sharma, B. P. Singh, H. D. Bhardwaj, R. Kumar, K. S. Golda, and R. Prasad, *Phys. Rev. C* **70**, 044606 (2004).
 - [19] D. Singh, R. Ali, M. A. Ansari, M. H. Rashid, R. Guin, and S. K. Das, *Phys. Rev. C* **79**, 054601 (2009).
 - [20] D. P. Singh Unnati, P. P. Singh, A. Yadav, M. K. Sharma, B. P. Singh, K. S. Golda, R. Kumar, A. K. Sinha, and R. Prasad, *Phys. Rev. C* **81**, 054607 (2010).
 - [21] P. D. Croft and K. Street Jr., *Phys. Rev.* **165**, 1375 (1968).
 - [22] R. Bimbot, D. Gardes, and M. F. Rivet, *Nucl. Phys. A* **189**, 193 (1972).
 - [23] R. N. Sagaidak, V. K. Utyonkov, and F. Scarlassara, *Nucl. Instrum. Methods Phys. Res., Sect. A* **700**, 111 (2013).
 - [24] D. J. Parker, P. Vergani, E. Gadioli, J. J. Hogan, F. Vettore, E. Gadioli-Erba, E. Fabrici, and M. Galmarini, *Phys. Rev. C* **44**, 1528 (1991).
 - [25] W. Reisdorf, *Z. Phys. A* **300**, 227 (1981); W. Reisdorf and M. Schädel, *ibid.* **343**, 47 (1992).
 - [26] R. Joosten, J. Powell, F. Q. Guo, P. E. Haustein, R.-M. Larimer, M. A. McMahan, E. B. Norman, J. P. O'Neil, M. W. Rowe, H. F. VanBrocklin, D. Wutte, X. J. Xu, and J. Cerny, *Phys. Rev. Lett.* **84**, 5066 (2000).
 - [27] J. F. Ziegler, *Appl. Phys. Lett.* **31**, 544 (1977); *Nucl. Instrum. Methods* **168**, 17 (1980).
 - [28] J. M. Anthony and W. A. Lanford, *Phys. Rev. A* **25**, 1868 (1982).

- [29] Stopping Power of Matter for Ions, <https://www-nds.iaea.org/stopping/>
- [30] F. Hubert, H. Delagrangé, and A. Fleury, *Nucl. Phys. A* **228**, 415 (1974).
- [31] R. L. Hahn, P. F. Dittner, K. S. Toth, and O. L. Keller, *Phys. Rev. C* **10**, 1889 (1974).
- [32] A. G. Demin, V. A. Druin, Yu. V. Lobanov, R. N. Sagaidak, and V. K. Utenkov, *Sov. J. At. Energy* **57**, 637 (1984).
- [33] M. Dasgupta, P. R. S. Gomes, D. J. Hinde, S. B. Moraes, R. M. Anjos, A. C. Berriman, R. D. Butt, N. Carlin, J. Lubian, C. R. Morton, J. O. Newton, and A. Szanto de Toledo, *Phys. Rev. C* **70**, 024606 (2004).
- [34] E. García-Toraño and M. L. Aceña, *Nucl. Instrum. Methods* **185**, 261 (1981).
- [35] L. Corradi, B. R. Behera, E. Fioretto, A. Gadea, A. Latina, A. M. Stefanini, S. Szilner, M. Trotta, Y. Wu, S. Beghini, G. Montagnoli, F. Scarlassara, R. N. Sagaidak, S. N. Atutov, B. Mai, G. Stancari, L. Tomassetti, E. Mariotti, A. Khanbekyan, and S. Veronesi, *Phys. Rev. C* **71**, 014609 (2005).
- [36] R. N. Sagaidak and A. N. Andreyev, *Phys. Rev. C* **79**, 054613 (2009).
- [37] NuDat 2.7, http://www.nndc.bnl.gov/nudat2/indx_dec.jsp
- [38] R. Bimbot and D. Gardes, *Nucl. Instrum. Methods* **109**, 333 (1973).
- [39] F. Gruner and F. Bell, *Phys. Rev. A* **72**, 024902 (2005).
- [40] C. M. Frey, G. Dollinger, A. Bergmaier, T. Faestermann, and P. Maier-Komor, *Nucl. Instrum. Methods Phys. Res., Sect. B* **107**, 31 (1996).
- [41] R. N. Sagaidak, N. A. Kondratiev, L. Corradi, E. Fioretto, T. Mijatovic, G. Montagnoli, F. Scarlassara, A. M. Stefanini, and S. Szilner, *Phys. Rev. C* **97**, 054622 (2018).